JOURNAL OF CATALYSIS **167,** 77–91 (1997)
ARTICLE NO. CA971591

Structure/Function Relationships in Nd_2O_3-Doped MgO Catalysts for the Methane Coupling Reaction

Andrew Burrows,* Christopher J. Kiely,* Graham J. Hutchings,† Richard W. Joyner,‡ and Mikhail Yu. Sinev§

*Department of Materials Science and Engineering, University of Liverpool, Liverpool, Merseyside L69 3BX, UK; †Leverhulme Centre for Innovative Catalysis, University of Liverpool, Liverpool, Merseyside L69 3BX, UK; ‡Catalysis Research Centre, Nottingham Trent University, Clifton Lane, Nottingham NG11 7NS, UK; and §Institute of Chemical Physics, Russian Academy of Sciences, Kosygina St. 4, Moscow 117334, Russia

Received March 22, 1996; revised November 21, 1996; accepted December 23, 1996

MgO doped with Nd_2O_3 has been evaluated as a catalyst for the oxidative coupling of methane (OCM) reaction. It is demonstrated that significant improvements in methane conversion efficiency and selectivity to C_2 products (as compared to pure MgO) can be achieved. The level of catalytic improvement is shown to be dependent on the Nd_2O_3 concentration and the precise catalyst preparation method. Detailed transmission electron microscopy studies have been performed on the Nd_2O_3/MgO catalysts prepared by an impregnation route and by a number of coprecipitation methods. Six distinct neodymia morphologies on the MgO support have been identified. These are (i) crystalline thin films, (ii) Nd_2O_3 crystallites attached to the MgO support, (iii) isolated Nd_2O_3 needles, (iv) epitaxial microclusters, (v) disordered thin films, and (vi) isolated clusters. The relative proportions of these Nd_2O_3 morphologies in the catalysts are also shown to depend upon the neodymia loading and the preparation route. Cross-correlation between microstructural observations and catalytic performance data for these materials enable us to deduce that the disordered neodymia films, which probably contain some dissolved Mg^{2+} ions, are largely responsible for the improvement in OCM performance.

1. INTRODUCTION

The finite quantities of crude oil and our escalating rate of oil consumption have created a need to develop alternative fuel technologies. One huge natural resource which remains largely untapped is natural gas. This potential resource has not been fully utilized because the largest reserves are located in some of the more remote regions of the world (1). The transportation costs of methane to highly populated areas for subsequent reprocessing are prohibitive and so considerable effort has been expended in the search for cost-effective on-site processes to convert methane into more useful products. One such possibility is the oxidative coupling of methane (OCM) to produce C_2 hydrocarbons. Early observations (2–4) that most simple oxides display some catalytic activity for this reaction have spurred many researchers to work on this particular problem. Kalenik and Wolf (5) have categorized the oxides useful in OCM as (i) MgO and Lipromoted MgO, (ii) lanthanide oxides, and (iii) transition metal oxides. The diversity of materials investigated and the wide range of experimental conditions used precludes a definitive explanation (thus far) on the exact nature of the reaction. However, recent reviews on methane coupling (4, 6) indicate that there is general agreement the reaction proceeds via homolytic cleavage of the CH_4 molecule at the catalyst surface to yield methane radicals. These subsequently react in the gas phase with other methyl radicals to form the C_2 products ethane and ethene. The former process is the rate limiting step and the reactions are said to be heterogeneous/homogeneous in character.

More recently, researchers have been begun to recognize the importance of catalyst morphology for the OCM reaction. Early studies on Sm_2O_3 catalysts indicated that different polymorphs could give rise to different catalytic performances (7, 8). Furthermore, Le Van *et al.* (9) demonstrated that the morphology of La_2O_3 has an important effect on the catalytic performance for methane activation. Hargreaves *et al.* (10–12) have evaluated the effect of microstructural variations on OCM performance in pure MgO and Li-doped MgO catalyst systems. One aspect of these latter studies was to explore the extent to which the reaction occurs at corner and edge sites on faceted {100} MgO surfaces. MgO samples with very different morphologies were prepared by a variety of methods (e.g., burning Mg ribbon in air, thermally decomposing magnesium hydroxide and magnesium carbonate). These were then assessed for catalytic performance and subsequently examined using transmission electron microscopy. Although the samples produced displayed hugely differing densities of corner and step sites, their *specific catalytic activities* (i.e., the rate of change of conversion of methane per unit surface area of catalyst) were the same. It was, suggested, and

[1] To whom correspondence should be addressed. Fax: 0151 794 4675. E-mail: ab0895@liv.ac.uk.

0021-9517/97 $25.00

subsequently confirmed by theoretical calculations (13), that vacancies on the planar surfaces of MgO are likely to be the active sites for methane activation.

The performance of MgO may be improved in a number of ways, one of the simplest being the addition of 5 wt% of lithium carbonate (11, 12, 14). As well as markedly increasing the selectivity of the catalyst to the desired C_2 products, it also causes a significant decrease in the surface area of the catalyst. Microstructural examination of the lithium-doped material demonstrated that the MgO grains, unlike the pure material, contained significant densities of $1/2\langle 100\rangle$ dislocations (11). The emergence points of these dislocations on the MgO surface were postulated as additional active sites since Li^+ ions segregated to the dislocation core could give rise to active $[Li^+O^-]$ centers, proposed earlier by Lunsford *et al.* (14).

Otsuka *et al.* (15) demonstrated in 1985 that Nd_2O_3 was another oxide which could be used to catalyze the OCM reaction. Furthermore, Sinev *et al.* (16) and Burrows *et al.* (17) demonstrated that if MgO was doped with small amounts of Nd_2O_3 an OCM catalytic performance could be achieved which was far superior to that of either of the pure oxides. The *synergistic* Nd_2O_3/MgO system is the subject of the current investigation.

In this study, a systematic series of mixed oxide samples have been prepared by impregnation of ex-hydroxide MgO with between 0.003 and 3.0 at.% neodymia. A further parallel series of Nd_2O_3-doped MgO samples prepared by coprecipitation methods has also been generated. Laboratory microreactor studies have then been used to investigate how methane conversion efficiency and C_2 selectivity depend on (i) the precise catalyst preparation route and (ii) the neodymia concentration. High resolution electron microscopy (HREM) has been carried out on the same samples to study the way in which the neodymia is dispersed on the MgO support. X-ray photoelectron spectroscopy has also been employed to estimate the surface neodymia coverage. Finally, cross-correlations between our microstructural observations and catalytic performance data have been attempted in order to elucidate the nature of the structure/function relationships in this system.

2. EXPERIMENTAL

2.1. Catalyst Preparation

Two series of Nd_2O_3 on MgO catalysts were studied. To provide a baseline for catalytic performance, pure MgO was prepared by thermally decomposing $Mg(OH)_2$ at 600°C (denoted as ex-OH). Series 1 catalysts were prepared by impregnation of ex-OH MgO with Nd_2O_3 using a 1 mol liter^{-1} nitrate solution (prepared by dissolving Nd_2O_3 in concentrated nitric acid and adding distilled water to give the above concentration). Impregnation was carried out repeatedly until the required neodymia loading was achieved. In atomic percent, these loadings were 0.003, 0.03, 0.3, and 3.0. The catalysts were dried at 150°C followed by calcination in air at 850°C.

Series 2 catalysts were prepared via three distinct coprecipitation routes designated ex-nitrate, ex-hydroxide, and ex-carbonate. Series 2 materials were all prepared with 0.3 at.% neodymia, since this concentration was judged to be the optimum doping level for catalytic improvement in the Series 1 catalysts. The *ex-nitrate* sample was prepared by decomposition of the dried residue of a mixed magnesium–neodymium nitrate solution. The *ex-hydroxide* sample was obtained by thermally decomposing the material precipitated as a mixed hydroxide from the previously described mixed nitrate solution using ammonium hydroxide. Similarly, the *ex-carbonate* sample was derived from thermal decomposition of the material precipitated as a mixed carbonate from the mixed nitrate solution using ammonium carbonate. All Series 2 samples were given a final calcination in air at 850°C.

2.2. Catalyst Testing

Catalysts were evaluated for the oxidative coupling of methane using a fixed-bed laboratory microreactor constructed from quartz glass. The method of catalyst testing has previously been described (10) and utilizes a catalyst bed mass of 0.06 g and on-line gas chromatographic analysis. The catalyst was exposed to a mixture of methane, oxygen, and argon in the ratio 15 : 5 : 80 (flow rate 50 cm^3 min^{-1}) at a total pressure of 1 bar and temperature of 750°C.

2.3. Microstructural Characterization

Magnesium oxide adopts the cubic sodium chloride type structure with a lattice parameter of 0.420 nm. It belongs to the space group *Fm3m* and has Mg^{2+} ions situated at (0, 0, 0) and O^{2-} ions situated at (1/2, 1/2, 1/2). MgO contains four molecular units per unit cell.

Neodymium oxide, Nd_2O_3, is a rare earth sesquioxide which is isostructural with La_2O_3. It can exist in either hexagonal or cubic polymorphic forms (18). The hexagonal phase has $a = 0.383$ nm and $c = 0.599$ nm and contains one molecular unit per unit cell. It belongs to the *P3̄m1* spacegroup and has atomic coordinates defined by

$$\begin{aligned} &\text{Nd: } (1/3, 2/3, z), && \text{where } z = 0.235\\ &O_a\text{: } (0, 0, 0)\\ &O_b\text{: } (1/3, 2/3, z), && \text{where } z = 0.630. \end{aligned}$$

The cubic form of Nd_2O_3 has a lattice parameter of 1.1048 nm and contains 16 molecular units per unit cell. Its atomic positions are defined by the equivalent positions

of the *Ia3* space group as follows:

Nd_a: (1/4, 1/4, 1/4)

Nd_b: $(x, 0, 1/4)$, where $x = 0.97$

O: (x, y, z), where $x = 0.385$, $y = 0.145$, and $z = 0.380$.

In this paper we specify the planes and zone axes of the hexagonal Nd_2O_3 crystal system using a primitive unit cell and the three-digit (*hkl*) Miller index convention.

For transmission electron microscopy analysis, the catalyst powder was dispersed onto lacey carbon film supported on a Cu-mesh grid. All microscopy studies were carried out on a JEOL 2000EX high resolution electron microscope operating at 200 kV. Fourier transform analysis of lattice fringe patterns from individual particles were carried out by scanning the image into a Macintosh Quadra computer and utilizing the NIH-image software package. Energy dispersive X-ray (EDX) spectra for local composition analysis were obtained in a VG HB601 UX scanning transmission electron microscope (STEM).

XPS experiments were carried out at room temperature and at 10^{-8} Torr on a VG ESCA3 spectrometer using Mg K_a X-radiation. Nd $3d_{5/2}$ and Mg 2s core level electron binding energies were calibrated relative to the C 1s line (285.0 eV). In order to obtain a quantitative analysis of the $[Nd]_{surface}$ to $[Mg]_{surface}$ concentration, the values of photoelectric cross sections cited by Scofield (19) were used. In subsequent calculations it is assumed that the composition of the surface layer probed by XPS (~3 nm) is uniform. While electron microscopy demonstrates that this is not the case, the use of more sophisticated models seems unjustified as they are unlikely to lead to dramatically different conclusions. The XPS results are used only as an indication of trends.

3. RESULTS

3.1. Catalyst Performance

The catalytic performance data of the Series 1 catalysts are shown in Table 1. Compared to pure MgO, the Nd_2O_3 on MgO catalysts perform significantly better in terms of CH_4 conversion efficiency and selectivity to C_2 hydrocarbons. Methane conversion increases gradually from the 0.6% displayed by pure MgO up to 24.2% for the 3 at.% Nd_2O_3/MgO catalyst. It is useful to note that the space velocities employed are significantly greater than in many OCM studies; thus conversions are often quite low. Nevertheless, the most significant increase in conversion efficiency occurs between the Nd_2O_3 loading of 0.03 and 0.3 at.%. Exactly the same trend is observed for selectivity to C_2 hydrocarbon formation which for pure MgO is 18% with the most significant increase up to 39.5% occurring for the 0.3 at.% Nd_2O_3/MgO sample. Given that the surface area of pure MgO and all the Series 1 catalysts is very similar (i.e., about 15 $m^2\ g^{-1}$), it is clear that impregnation of MgO by Nd_2O_3 produces a significant promotional effect. Furthermore, it appears that a neodymia loading of about 0.3 at.% is critical since at this level the most significant improvements in CH_4 conversion efficiency and C_2 selectivity are attained. Measurements of the $[Nd]_{surface}/[Mg]_{surface}$ concentrations as deduced from XPS experiments are also presented in Table 1. These ratios have been calculated assuming that the composition of the region sampled by XPS 3 is homogeneous. Neodymium could be detected on the surface even at low impregnation levels, suggesting that it has a tendency to remain on the MgO surface. The general trend observed was that the higher the Nd_2O_3 loading level the higher was the $[Nd]_{surface}/[Mg]_{surface}$ ratio.

TABLE 1

Catalytic Performance Data for Impregnated Series 1 Nd_2O_3/MgO Materials (0.06 g; 750°C; 1 bar; $CH_4 : O_2 : Ar = 15 : 5 : 80$; Flow Rate, 50 $cm^3\ min^{-1}$)

	Series 1 sample				
	Pure MgO	MgO/0.003 at.% Nd_2O_3	MgO/0.03 at.% Nd_2O_3	MgO/0.3 at.% Nd_2O_3	MgO/3.0 at.% Nd_2O_3
Surface area ($m^2\ g^{-1}$)	15	15	15	15	15
Grain size distribution (nm)	10–60	10–60	10–60	10–60	10–60
CH_4 conversion (%)	0.6	1.0	2.8	20.0	24.2
C_2 selectivity (%)	18.0	20.0	24.0	39.5	41.0
$[Nd]_{surface}/[Mg]_{surface}$	0	[a]	0.068	0.18	1.6

[a] Below detectability limit.

The catalytic performance data of the coprecipitated Series 2 catalysts is presented in Table 2. For comparative purposes the corresponding data for the impregnated (i.e., Series 1) 0.3 at.% Nd_2O_3/MgO sample is also shown. The Series 2 catalysts are less active in comparison with the Seires 1 catalyst, probably as a consequence of the consistently lower surface area of the coprecipitated materials. In all cases, however, the C_2 selectivities of the Series 2 catalysts are higher than that of the corresponding Series 1 material. The highest C_2 selectivity (71.5%) was observed for the ex-carbonate coprecipitated sample. XPS characterization of the Series 2 material shows that the apparent surface neodymium concentration decreases markedly in the order ex-nitrate > ex-hydroxide > ex-carbonate. Care must be taken in inferring too much from the XPS data, however, since the surface areas of the three different coprecipitated samples also vary considerably (with the ex-nitrate sample having the lowest surface area).

3.2. Nd_2O_3 Morphologies

A TEM examination of all the Series 1 and Series 2 Nd_2O_3/MgO catalyst samples has revealed that the

TABLE 2

Catalytic Performance Data for Coprecipitated Series 2 Nd_2O_3/MgO Materials (0.06 g; 750°C; 1 bar; $CH_4 : O_2 : Ar = 15 : 5 : 80$; Flow Rates, 50 cm^3 min^{-1}

	Sample			
	MgO (ex-OH) 0.3 at.% Nd_2O_3 Impregnated (Series 1)	MgO (ex-nitrate) 0.3 at.% Nd_2O_3 Co-precipitated (Series 2)	MgO (ex-OH) 0.3 at.% Nd_2O_3 Co-precipitated (Series 2)	MgO (ex-carbonate) 0.3 at.% Co-precipitated Nd_2O_3 (Series 2)
Surface area (m^2 g^{-1})	15	2.5	7.7	5.0
Grain size distribution (nm)	10–60	200–1500	50–250	200–500
CH_4 conversion (%)	20.0	10.6	10.1	8.7
C_2 selectivity (%)	39.5	59.0	63.0	71.5
$[Nd]_{surface}/[Mg]_{surface}$	0.18	0.66	0.46	0.16

neodymia can adopt six distinct morphologies. Before going on to show how the occurrence and frequency of these depend upon catalyst preparation method and Nd_2O_3 loading, it is worth presenting a brief microstructural analysis of these six neodymia morphologies individually.

3.2.1. Crystalline thin films. Figure 1a shows an example of an extended crystalline thin film of neodymia supported on the {100} MgO surface. The lateral dimensions of these films rarely exceed 15×15 nm and profile imaging experiments suggests that they are less than 1.5 nm in thickness. The Fourier transform (FT) obtained from this particular crystalline patch is presented in Fig. 1b and is consistent with the $[\bar{2}21]$ zone axis of the hexagonal form of Nd_2O_3 as shown schematically in Fig. 1c. All extended crystalline Nd_2O_3 films analyzed in this way were found to match only to the hexagonal neodymia phase.

3.2.2. Crystallites attached to the MgO support. In samples loaded with more than 0.03 at.% Nd_2O_3, cylindrical needles of crystalline material were sometimes found to be growing perpendicularly outward from the {100} MgO surface. A typical example of such a protruding crystallite, about 20 nm in length, is illustrated in Fig. 2a. Fourier transform analysis of the fringe periodicities and angles from all such cylindrical crystallites showed them to be consistent with the cubic form of neodymia. For the particular example shown, the crystal is oriented along the $[2\bar{5}4]$ zone axis as demonstrated by the FT and diffraction pattern analysis as shown in Figs. 2c and 2b, respectively. A second similar morphology in which the protrusions are more spherical in character (Fig. 3a) was also occasionally observed in the more heavily doped samples. These all matched to the hexagonal neodymia phase, and in the particular case shown, to the $[0\bar{1}1]$ hexagonal zone axis (Figs. 3b and 3c). Energy dispersive X-ray analysis performed on both of these protruding crystallite types (using a 1.5-nm-diameter electron probe in a STEM) indicated they did not contain any dissolved Mg^{2+} ions at the EDX detectability limit of 0.1 at.%.

3.2.3. Isolated needles. In samples with neodymia loadings $\geq$3 at.%, isolated needles of Nd_2O_3 were commonly observed. A typical example of this morphology type is presented in Fig. 4(a), where a needle 250 nm in length and 50 nm diameter is clearly visible. Convergent beam electron diffraction patterns from such crystals (Fig. 4b) have allowed us to deduce that they have the hexagonal Nd_2O_3 crystal structure. Again STEM-EDX analysis suggest that the Mg^{2+} ion content, if any, of these isolated needles is below the EDX detectability limit.

3.2.4. Epitaxial microclusters. This morphology is typified by the image shown in Fig. 5 in which three Nd_2O_3 clusters (with projected pseudohexagonal symmetry) are arrowed. The MgO crystallite is oriented close to the $[0\bar{1}1]$ zone axis in this image. In terms of lateral dimensions, these three represent the typical size range found for neodymia in this form, i.e., 1×1 nm to 2.5×2.5 nm. The common orientation of the clusters with respect to the substrate indicates that an epitaxial relationship exists between the two crystal structures. Detailed analysis of such images [20] suggests that the epitaxial relationship between the MgO support and Nd_2O_3 microcluster is probably as follows:

$$MgO[001] // Nd_2O_3^{cubic}[001] \quad \text{and}$$

$$MgO[110] // Nd_2O_3^{cubic}[100].$$

This means that the (001) Nd_2O_3 plane connects to the (001) MgO plane with a 45° rotation about [001] between the two unit cells as shown schematically in Fig. 6. Under these conditions there is only a 6.75% lattice mismatch between the two lattices. Examination of the Nd_2O_3 crystal structure along [001] shows that the microcluster must be at least half a unit cell thick (i.e., 0.5524 nm) in order to give rise to the projected Nd atom arrangement as observed in Fig. 5. However, since these clusters are very difficult to observe in profile (see the MgO facet surfaces in Fig. 5) we also believe that they are less than one unit cell in thickness. Hence, the microcluster thickness is likely to be between

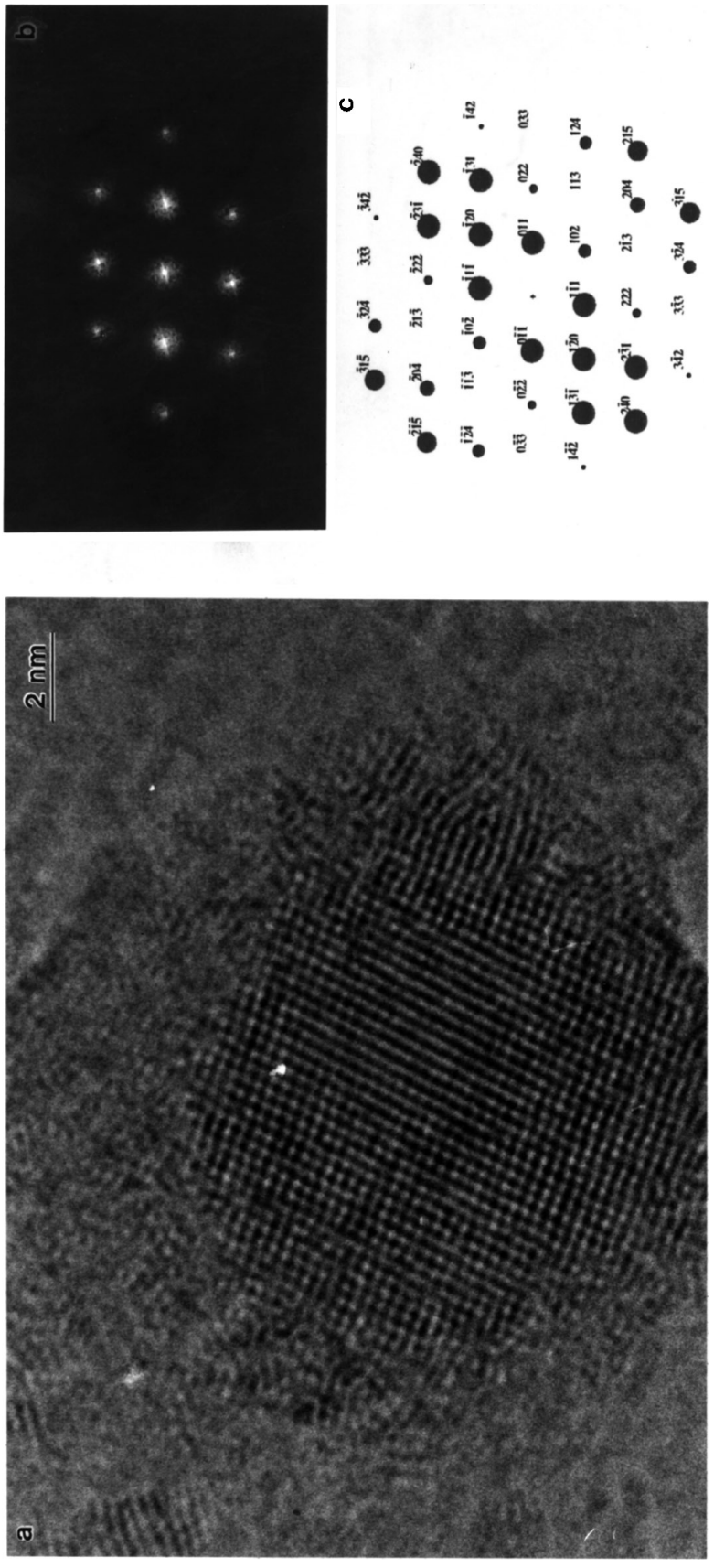

FIG. 1. Lattice image (a), corresponding FT (b), and schematic diffraction pattern (c) from a crystalline thin film of hexagonal Nd_2O_3 oriented along the $[\bar{2}\bar{2}1]$ zone axis.

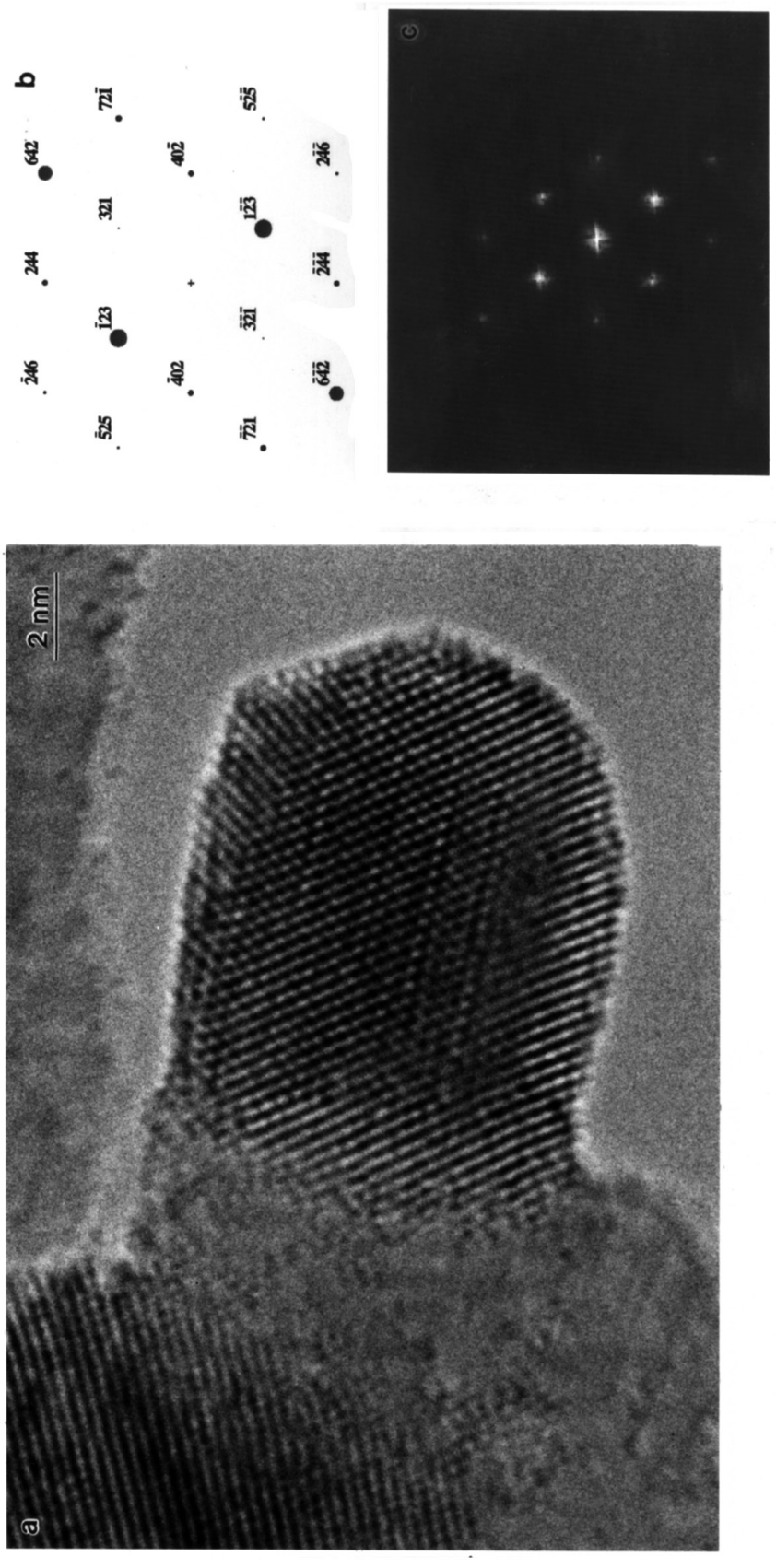

FIG. 2. Lattice image (a), corresponding FT (c), and schematic diffraction pattern (b) from a cubic Nd_2O_3 needle (oriented along the $[2\bar{5}4]$ zone axis) which is attached to the MgO support.

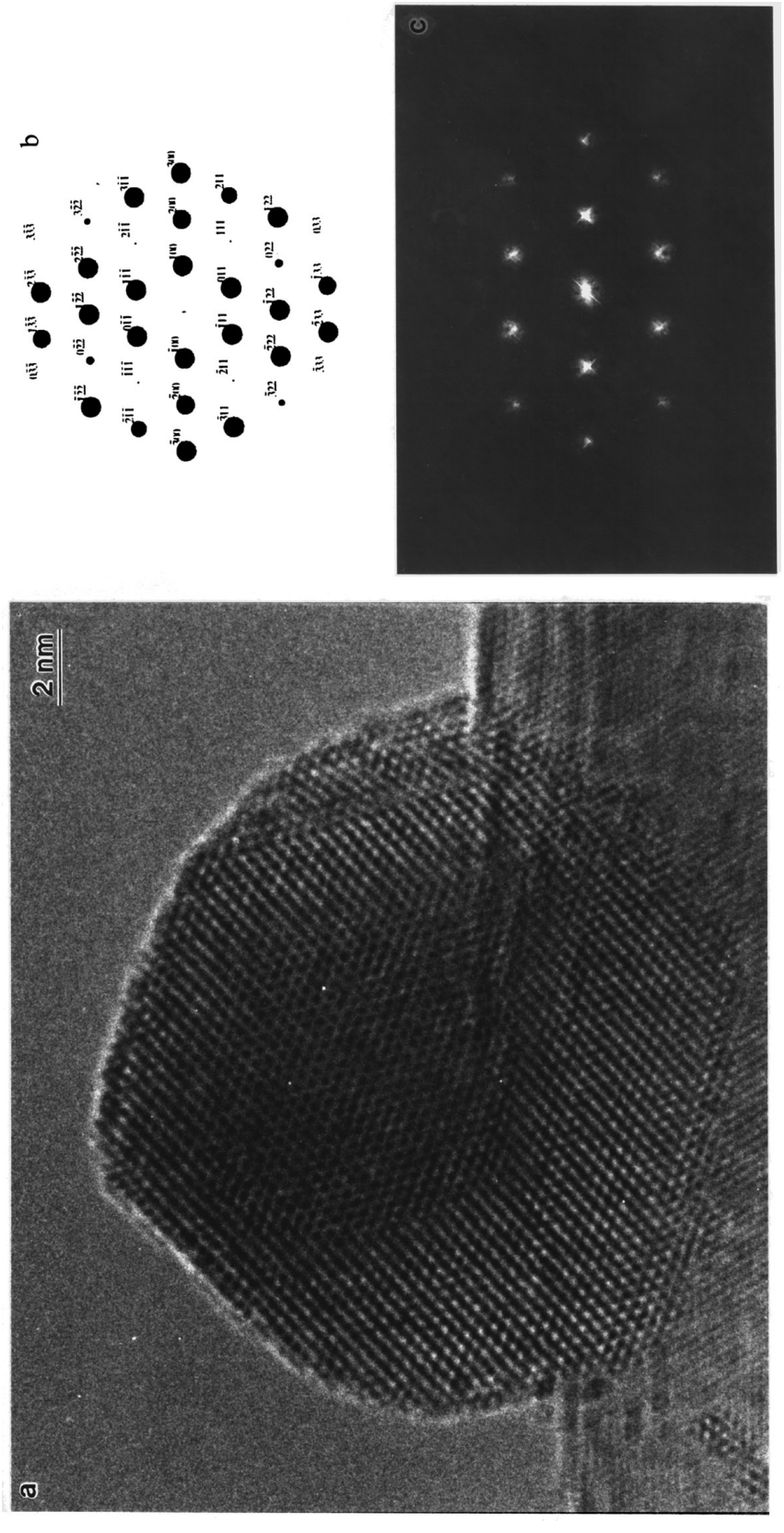

FIG. 3. Lattice image (a), corresponding FT (c), and schematic diffraction pattern (b) from a hexagonal Nd_2O_3 needle (oriented along the $[01\bar{1}]$ zone axis) which is attached to the MgO support.

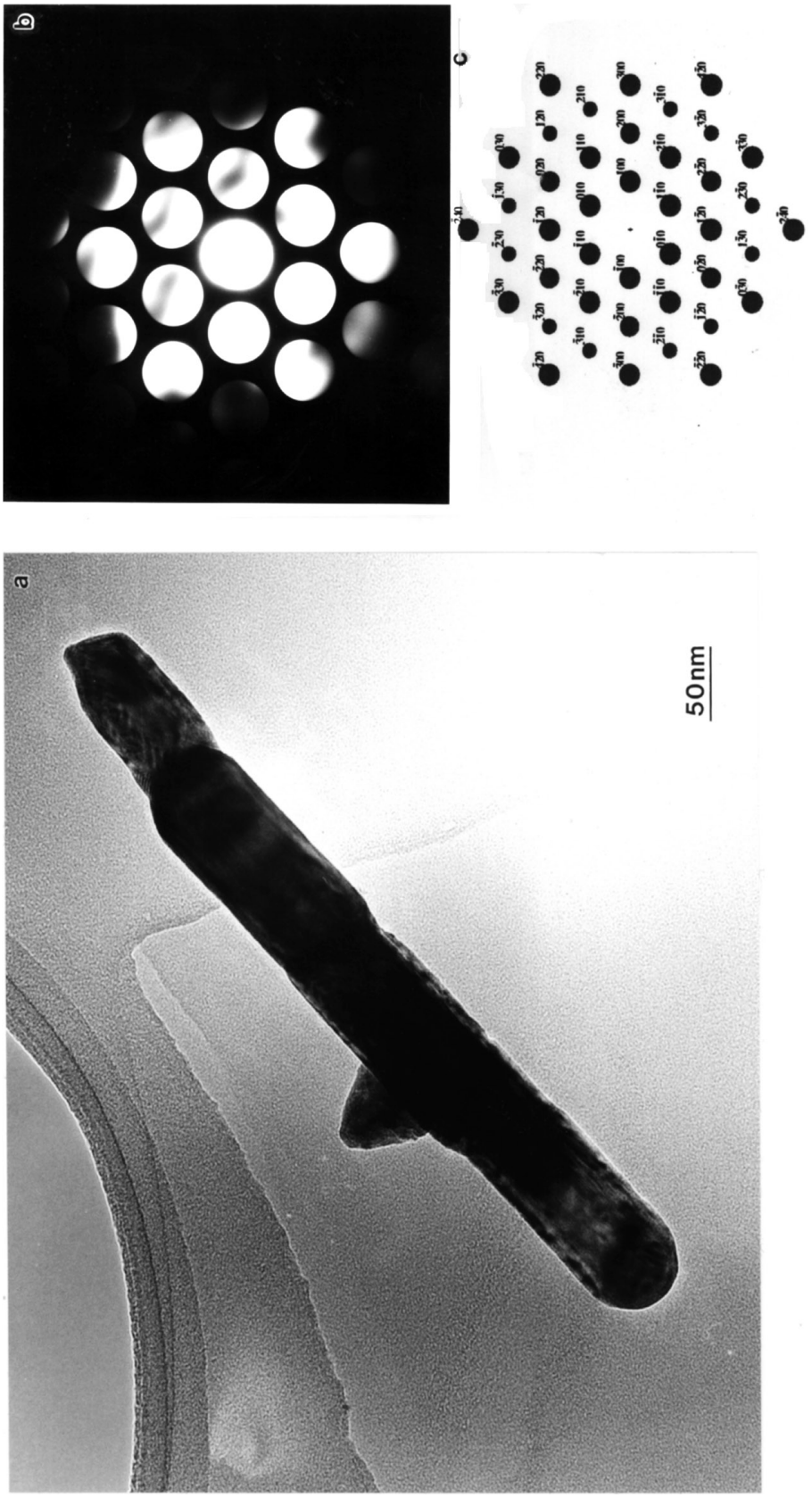

FIG. 4. Bright field image of an isolated needle of neodymia (a), its corresponding Convergent Beam Electron Diffraction pattern (b) and the simulated diffraction pattern for [001] hexagonal Nd_2O_3.

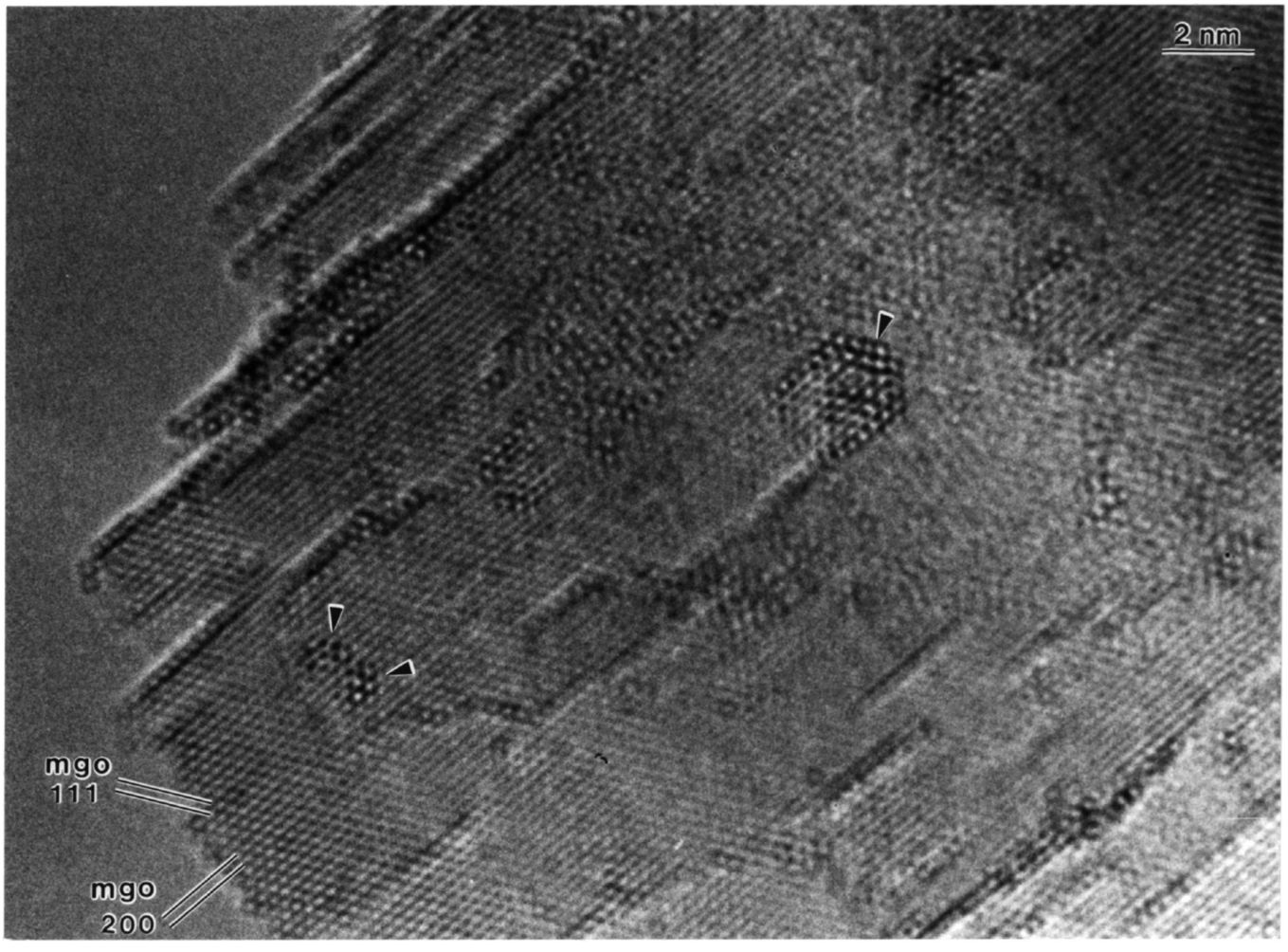

FIG. 5. HREM image of epitaxial Nd_2O_3 microclusters on an MgO support which is oriented close to the $[0\bar{1}1]$ zone axis.

0.55 and 1.1 nm. The lateral extent of the clusters may be limited to less than 4 nm since it is anticipated that this is the critical size at which a misfit dislocation would be required to relieve the elastic strain energy generated by matching the microcluster pseudomorphically onto the rigid MgO support.

3.2.5. Disordered thin films. Disordered thin films of neodymia have been found to occur to varying degrees in all of the samples studied. A good example is shown in Fig. 7, where the layer (which is about 2 nm thick) is seen in profile and effectively smooths out the faceted nature of the MgO surface. The typical areas covered by such disordered patches can be anything between 3×3 nm and 25×25 nm depending on the specimen loading. Attempts to find out whether or not such "glassy" overlayers contain any dissolved Mg^{2+} ions have proved inconclusive. STEM-EDX analysis on the layers in profile always gives rise to an Mg signal but this could be generated by beam spreading effects as the electrons traverse the sample.

3.2.6. Individual neodymia clusters. Distinct dark spots or flecks of the type shown in Fig. 8 were commonly found scattered on the MgO {100} surfaces. They appear to be preferentially situated at the step edges and corner sites associated with the substrate facets. These dark spots remain visible irrespective of sample tilt although their contrast against the MgO support decreases as the MgO becomes more strongly diffracting. This suggests that in Fig. 8, where the MgO is tilted away from a Bragg condition, mass contrast is the dominant contrast mechanism in operation. These flecks, which have a diameter of around 0.2 nm, are thought to contain no more than one or two Nd atoms since the Nd^{3+} ion radius is only 0.11 nm.

3.3. Catalyst Microstructure, Series 1

Table 3 summarizes the distribution of neodymia morphologies observed in the impregnated Series 1 catalysts. It is possible for all six of the neodymia morphologies to coexist in the same sample, particularly in the catalysts with higher Nd_2O_3 loadings (i.e., 0.3 and 3 at.%). The attached

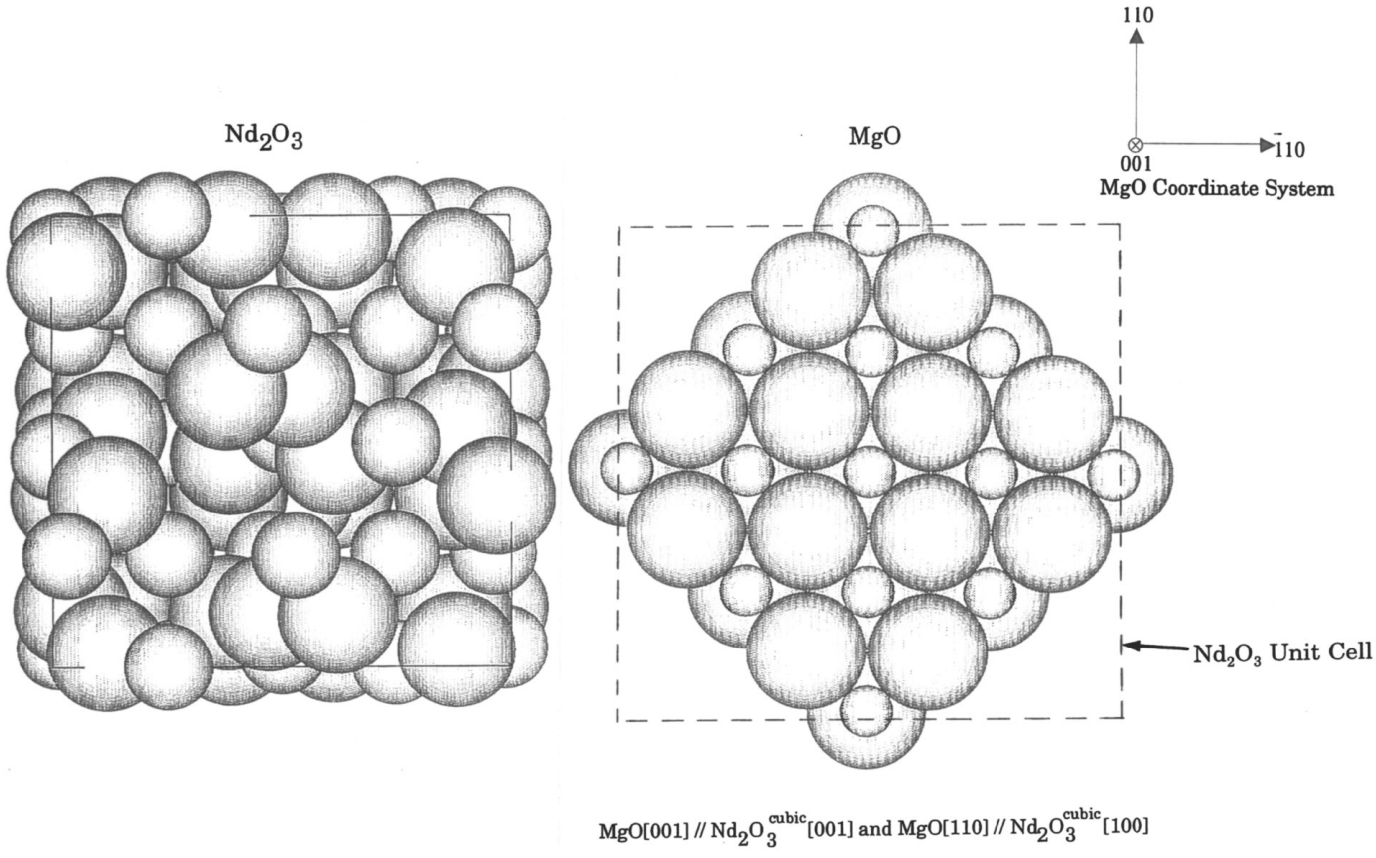

FIG. 6. Schematic diagram illustrating the nature of the epitaxial orientation relationship between the cubic Nd_2O_3 microclusters and the MgO support.

needle morphologies (both hexagonal and cubic) occurred frequently in the 0.3–3.0 at.% Nd_2O_3 doping range. The isolated needles of hexagonal Nd_2O_3 were numerous in the 3.0 at.% sample but quite rare in the 0.3 at.% doped catalyst.

The extended crystalline Nd_2O_3 films were also only found in the samples loaded with 0.3–3.0 at.% Nd_2O_3, whereas continuous disordered neodymia films are seen to varying degrees in *all* samples. They were even observed frequently in the sample with the lowest concentration (0.003 at.%) in patches approximately 3 nm in diameter. Increasing the concentration to 0.03 at.% results in larger patches (~6 nm in diameter) of disordered material. At the two highest concentrations the disordered film is commonly found in profile up to 10 nm in thickness and to cover areas of up to 25 nm in diameter. The epitaxial microclusters and individual cluster morphologies have been observed in all of the Series 1 catalyst materials. As might be expected, their frequency increases as a function of neodymia concentration.

An important point worthy of note is that the underlying MgO support morphology and particle size distribution was *identical* for all the catalysts in the Series 1 set. Furthermore, when unused and used catalyst materials at any particular Nd_2O_3 concentration were compared, no differences in morphology were ever detected. This indicates that the oxidative coupling reaction has had no effect on the morphology.

3.4. Catalyst Microstructure, Series 2

The MgO support in Series 2 catalysts exhibits a different morphology for each preparation route (an observation consistent with the microstructural studies of pure magnesium oxide catalysts performed by Hargreaves *et al.* (11). The ex-hydroxide MgO has a plate-like morphology with plate diameters varying between 50 and 250 nm. The ex-carbonate MgO particles are very irregular in shape and vary in size between 200 and 500 nm. The ex-nitrate MgO particles are almost "spherical" with a grain size distribution of 200–1500 nm. These observations are in general agreement with the surface area measurements on these materials (Table 2). The overriding common feature between these materials was that they all exposed {100}-type surface facets, albeit with greatly differing densities of step and corner sites. From a catalytic point of view, however, these low-coordination sites have been shown to be

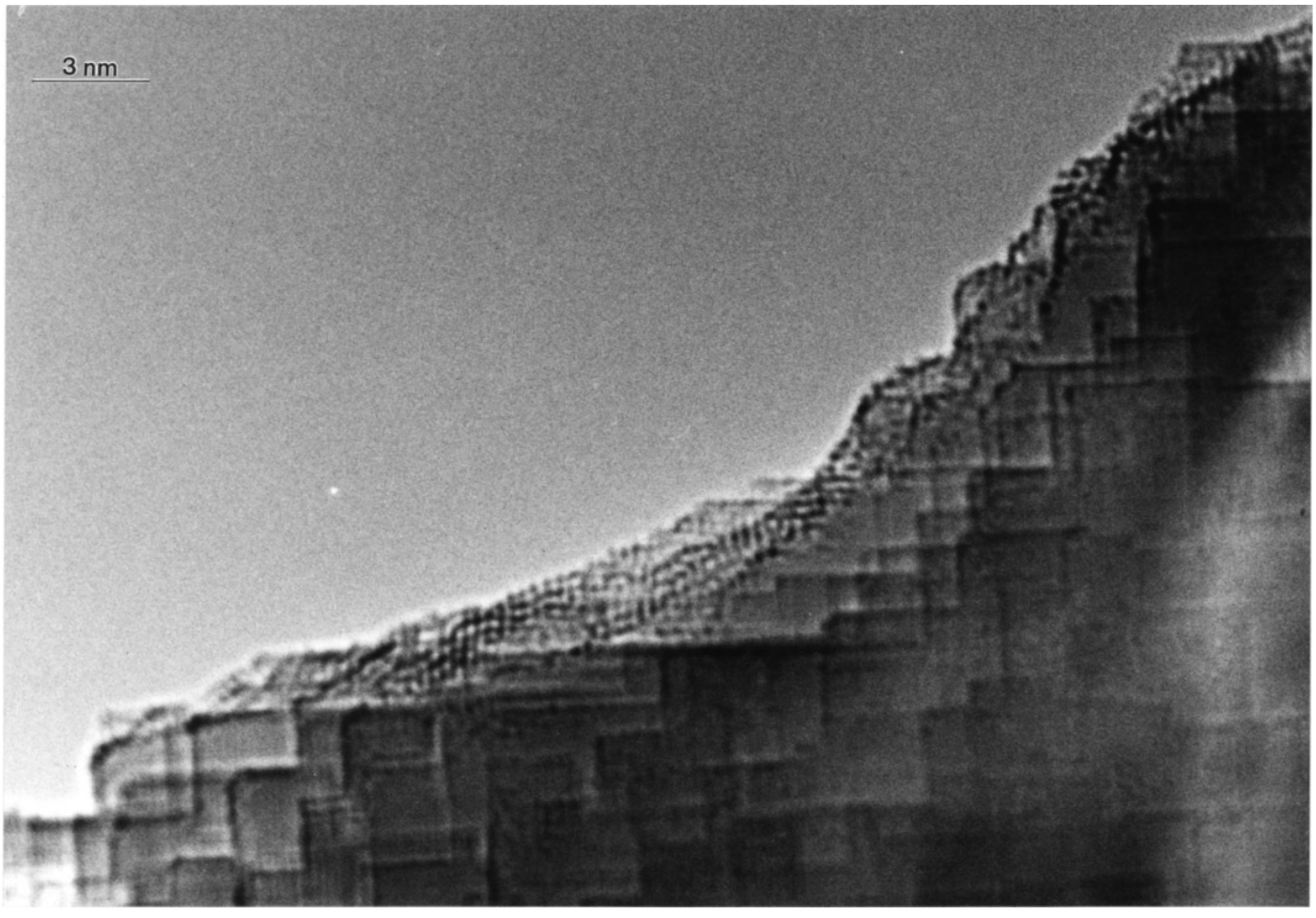

FIG. 7. HREM profile image showing a disordered thin film of neodymia coating the MgO (100) surface.

insignificant compared to vacancy sites on the (100) MgO surface for the oxidative coupling of methane reaction (11).

The neodymia morphology distribution for Series 2 catalysts is summarized in Table 4. In common with the Series 1 catalysts, no morphological differences could be found between samples in their used and unused states. Of the three types of coprecipitated samples studied, only the ex-carbonate material shows the wide range of Nd_2O_3 morphologies seen in the equivalent Series 1 catalyst, and even in this case there are notable differences. For instance, the two Nd_2O_3 needle morphologies are seen only very occasionally and those attached to the MgO surface always have the cubic Nd_2O_3 structure. In addition, no epitaxial microclusters were observed in this sample. The most commonly observed Nd_2O_3 morphologies in the ex-carbonate sample were the patches of disordered material, individual specks and extended crystalline thin films.

The dominant neodymia morphologies found in the ex-hydroxide and ex-nitrate samples were the disordered thin films. Neither showed evidence of Nd_2O_3 needles (attached or isolated) nor of extended crystalline thin films. Individual flecks were commonly seen in both samples, whereas the occasional epitaxial microcluster was seen in the ex-nitrate material.

4. DISCUSSION

The results clearly demonstrate that doping MgO with Nd_2O_3 gives a significant improvement of catalytic performance in the oxidative coupling of methane as compared to pure MgO in terms of specific activity. The level of improvement depends on both doping level and catalyst preparation route. Furthermore, a rich variety of possible Nd_2O_3/MgO morphologies have been demonstrated to exist. The results to be discussed below strongly suggest that there is a certain neodymia morphology (or combination of morphologies) on the MgO which is responsible for the increased catalytic activity and selectivity.

Before discussing the possible candidate morphologies responsible for this improvement, it is worthwhile pointing out that this study shows that the morphology of MgO doped with neodymia is quite different from the

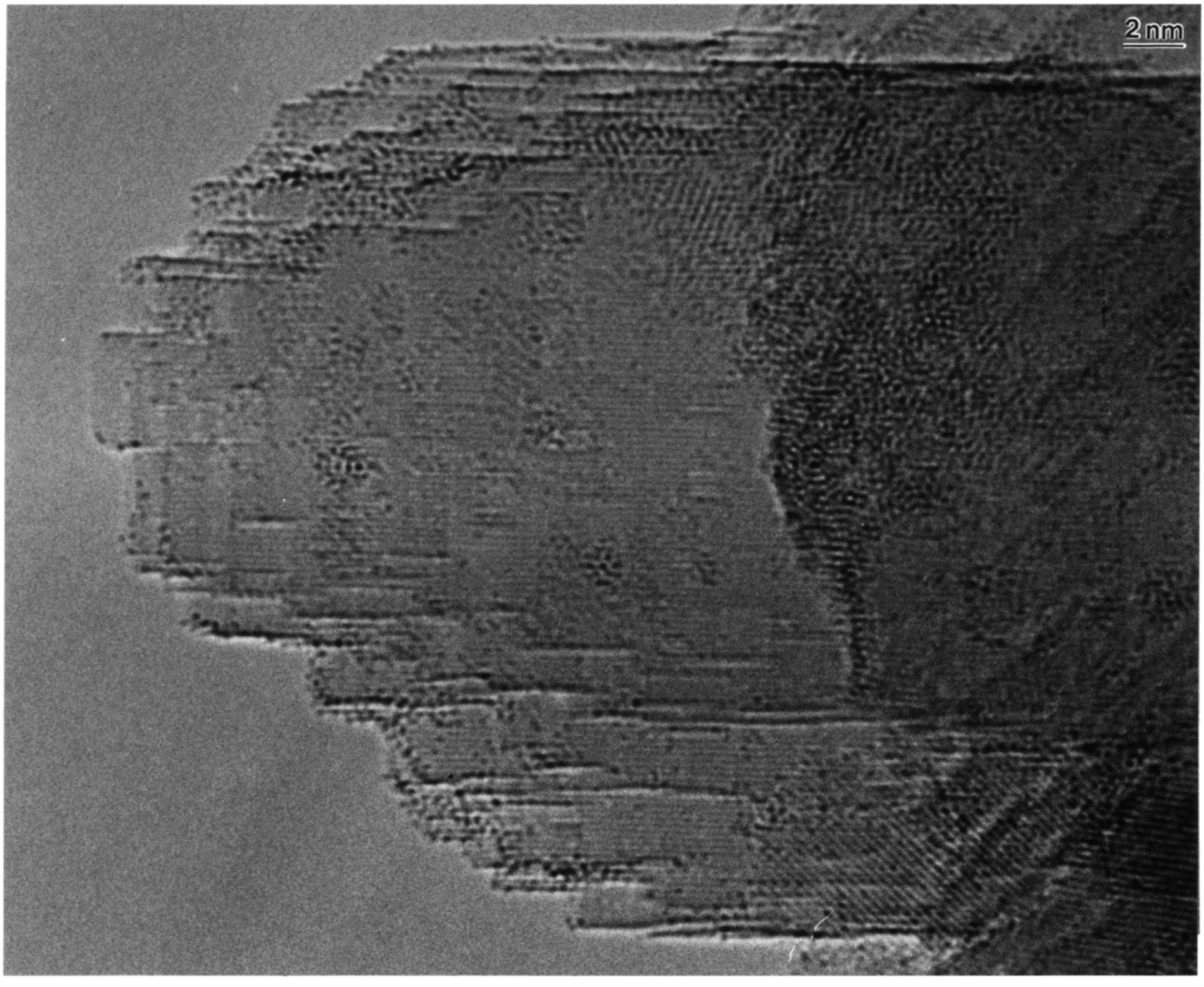

FIG. 8. HREM image showing individual flecks of neodymia on the MgO (100) surface.

situation when lithium or gold is used as the dopant (11, 12). Hargreaves *et al*. found that both these dopants cause significant MgO grain growth due to the substitution of Mg^{2+} cations with monovalent dopant cations. When substitution with Au^{+} or Li^{+} takes place, anion vacancies are introduced to maintain electroneutrality. This artificial increase in the vacancy population gives rise to an enhancement in self-diffusion coefficients. This results in an accelerated sintering rate as compared to pure MgO when the catalyst is prepared. No comparable effect occurs with Nd_2O_3 doping, as evidenced by the Series 1 catalysts, since the MgO grain size remains constant irrespective of the doping Nd_2O_3 level. This is not entirely surprising considering the difference in radius size of the Nd^{3+} and Mg^{2+} ions, which are 0.11 and 0.06 nm, respectively (21). Indeed, the proposition that there is no dissolution of Nd^{3+} in the MgO lattice has been confirmed by electron paramagnetic resonance measurements (16) and high spatial resolution STEM-EDX analysis (20). A second clear difference exists between Li-doped and Nd_2O_3-doped MgO materials. The former have been reported (11, 12) to generate significant densities of $1/2\langle 100\rangle$ dislocations within the MgO grains. The emergence sites of these dislocations on the MgO surface are thought to be active sites in the OCM reactions. No such line defects were ever generated by doping the MgO with Nd_2O_3.

Before considering which of the six observed morphologies contribute most to the increased conversion and selectivity of the neodymia/magnesia catalysts, it is important to recognize that neodymia itself has been identified as a promising OCM catalyst (15). We have studied the performance of both cubic and hexagonal phases of neodymia in the OCM reaction (22) and the results will be reported

TABLE 3

Summary of Microstructural Observations for Pure MgO and the Series 1 Impregnated Nd_2O_3/MgO Catalysts

		Series 1—(ex OH impregnated)/at.% Nd_2O_3				
Catalyst	Pure MgO ex-OH	0.003	0.03 Unused	0.03 Used	0.3	3.0
MgO morphology	Cubes (faceted)	Cubes (faceted)				
MgO grain size	10–60 nm	10–60 nm				
Nd_2O_3 needles attached to MgO (100) surface	—	X	X	X	✓ Cubic and hexagonal (20 × 10 nm)	✓ Cubic and hexagonal (20 × 10 nm)
Isolated crystalline Nd_2O_3 needles	—	X	X	X	✓ Hexagonal (occasional)	✓ Hexagonal (250 × 50 nm)
Extended crystalline Nd_2O_3 thin films	—	X	X	X	✓ (15 × 10 nm)	✓ (15 × 10 nm)
Epitaxial Nd_2O_3 microclusters	—	✓	✓	✓	✓	✓
Continuous disordered thin film of Nd_2O_3	—	✓	✓	✓	✓	✓
Individual Nd_2O_2 clusters	—	✓	✓	✓	✓	✓

in detail in a subsequent paper (23). However, it is clear that the performance of the two single oxide phases is poor compared to that of the mixed oxide materials, with both specific activities and C_2 selectivities markedly lower than for the best magnesia impregnated catalysts.

It is probable that the disordered neodymia thin film morphology is the most important in optimizing the catalytic performance of the Nd_2O_3/MgO catalysts. Evidence for this conclusion is provided by comparing the structural observations contained in Tables 3 and 4 with the catalytic performance data in Tables 1 and 2 and is supported by the results on the MgO impregnated materials, where the presence of a disordered neodymia phase is correlated with the improvement in catalytic performance (23).

The epitaxial microclusters have been discounted since they are common to all the Series 1 catalysts and are found only in the least selective sample of Series 2 (i.e., ex-nitrate). Individual Nd_2O_3 clusters have also been rejected on the basis that they are commonly present in all the catalyst samples studied.

Crystalline Nd_2O_3 in the form of cubic or hexagonal needles occurs in the more highly doped Series 1 catalysts, but rarely in the coprecipitated samples of Series 2. Nonetheless, all of the Series 2 catalysts are more selective than any of the Series 1 samples; the lower methane conversion efficiency of the Series 2 catalysts can be attributed to the lower surface area of these coprecipitated materials. Since pure crystalline cubic and hexagonal phases of Nd_2O_3 have previously been shown to perform poorly in the OCM reaction (22), it can be concluded that discrete crystals of Nd_2O_3 do not contribute *significantly* to the high activity and selectivity of Series 1 and 2 catalysts.

If the extended crystalline thin film were the morphology that determines the overall catalytic performance, then it would have been expected to found in all the Series 2 catalysts and yet it was not. It is therefore logical to conclude that the disordered thin film is the active surface that results in the improved catalytic performance for C_2 formation since it is present in all samples. A correlation also exists between the level of catalytic improvement and the *amount* of disordered phase present. For instance, the activity and C_2 selectivity of Series 1 material increases steadily until somewhere between 0.03 and 0.3 at.% of Nd_2O_3 has been added. At low doping levels, progressively greater surface coverage with disordered thin film material is achieved. At higher doping levels, much of the available additional neodymia goes into the bulk crystallites instead of the active disordered phase. This correlates with the observed leveling off of catalytic improvement between 0.3 and 3.0 at.% Nd_2O_3. Further evidence for the effectiveness of the disordered neodymia morphology comes from the fact that the highly selective Series 2 catalysts primarily exhibit "glassy" neodymia films.

Having identified a plausible active surface for the Nd_2O_3 on MgO catalysts, we must also consider the possibility that the active centers in the OCM reaction result from the dissolution of Mg^{2+} ions in the disordered neodymia thin films (a "reverse" doping effect). The dissolution of Mg^{2+} ions into ordered or disordered Nd_2O_3 films is certainly not precluded on the basis of the difference in cation size in this

TABLE 4

Summary of Microstructural Observations for the Series 2 Coprecipitated Nd_2O_3/MgO Catalysts

Catalyst	Series 2/0.3 at.% Nd_2O_3		
	Ex-nitrate	Ex-hydroxide	Ex-carbonate
MgO morphology	More spherical particles—{100} facets exposed	Platelike—{100} facets exposed	Irregular shaped particles—{100} facets exposed
MgO grain size	200–1500 nm	50–250 nm	200–500 nm
Nd_2O_3 needles attached to MgO (100) surface	X	X	✓ Cubic (occasional—20 × 10 nm)
Isolated crystalline Nd_2O_3 needles	X	X	✓ Hexagonal (occasional—250 × 50 nm)
Extended crystalline Nd_2O_3 thin films	X	X	✓ (15 × 10 nm)
Epitaxial Nd_2O_3 microclusters	✓ (Few)	X	X
Continuous disordered thin film of Nd_2O_3	✓ (Extensive coverage)	✓	✓
Individual Nd_2O_3 clusters	✓	✓	✓

instance. Furthermore, it is entirely plausible that the substitution of Mg^{2+} ions into Nd_2O_3 could serve to generate additional O^{2-} vacancy sites which would serve to improve the OCM selectivity. Catalysts prepared by the coprecipitation methods, having both Mg^{2+} and Nd^{3+} ions in solution together at the precursor stage, are more likely to produce such a microstructure and could therefore explain the superior selectivity of the Series 2 catalysts. Although we strongly suspect the presence of disordered Mg^{2+} in the neodymia films, high spatial resolution microanalysis experiments in a STEM have not produced definitive confirmation of such a reverse doping effect. This is because even though some magnesium is observed in EDX spectra this maybe an artifact picked up from the MgO support due to the ultrathin nature of the film and the presence of beam broadening effects.

5. CONCLUSIONS

Compared to pure MgO, the Nd_2O_3 on MgO materials catalyze the oxidative coupling of methane reaction significantly better in terms of CH_4 conversion efficiency and selectivity to C_2 hydrocarbons. The level of improvement is dependent on the doping concentration and the precise catalyst preparation method. The Nd_2O_3/MgO catalyst exhibiting the highest C_2 selectivity of 71.5% so far was the ex-carbonate coprecipitated sample.

Detailed transmission electron microscopy studies have shown that the neodymia can exist in six possible forms, namely (i) crystalline thin films, (ii) "bulk" crystallites attached to the MgO support, (iii) isolated needles, (iv) epitaxial microclusters, (v) disordered thin films, and (vi) individual clusters. The occurrence and relative abundances of these various forms of neodymia also depends on the doping concentration and precise preparation route. Careful cross-correlation between the microstructural observations and catalytic performance data has allowed us to establish a definite structure/function relationship in this Nd_2O_3/MgO catalyst system. We believe that the disordered glassy neodymia phase is the critical component for enhanced OCM catalyst performance. It is also highly probable that this disordered neodymia phase is stabilized and made even more active by the presence of dissolved Mg^{2+} ions. In-depth studies on the MgO-doped Nd_2O_3 catalyst system, in which we generate a structurally disordered cubic neodymia phase (22, 23) that is highly active and selective for OCM, support our proposal that the presence of a disordered and impure "glassy" neodymia phase is most effective in enhancing OCM performance. Further implications of the results from the study on the MgO-doped Nd_2O_3 catalysts will be discussed in a subsequent paper (23).

ACKNOWLEDGMENTS

We thank the Royal Society and EPSRC for their financial support of this work. Useful discussions with Dr. J. S. J. Hargreaves, Mr. R. W. Devenish, and Dr. Y. P. Tyulenin are also gratefully acknowledged.

REFERENCES

1. Parkyns, N. D., *Chem. Br.* **26**, 841 (1990).
2. Ito, T., and Lunsford, J. H., *Nature* **314**, 721 (1985).
3. Keller, G. E., and Bhasin, M. M., *J. Catal.* **73**, 9 (1982).
4. Hutchings, G. J., Scurrell, M. S., and Woodhouse, J. R., *J. Chem. Soc. Faraday Trans.* **85**, 2507 (1989).

5. Kalenik, K., and Wolf, E. E., *Catal. R. Soc. Chem*. **10**, 154 (1993).
6. Lunsford, J. H., *Catal. Today* **6**, 235 (1990).
7. Korf, S. J., Roos, J. A., Diphoorn, J. M., Veehof, R. H. J., van Ommen, J. G., and Ross, J. R. H., *Catal. Today* **4**, 279 (1989).
8. Skolovski, V. D., Bevskaya, D. V., Plyasov, L. M., Litvak, and Uvaraov, N. Ph., *Catal. Today* **6**, 489 (1990).
9. Le Van, T., Che, M., Kermarec, M., Louis, C., and Tatibouet, J. M., *Catal. Lett.* **6**, 395 (1990).
10. Hargreaves, J. S. J., Hutchings, G. J., and Joyner, R. W., *Stud. Surf. Sci. Catal.* **61**, 155 (1991).
11. Hargreaves, J. S. J., Hutchings, G. J., Joyner, R. W., and Kiely, C. J., *J. Catal.* **135**, 576 (1992).
12. Hargreaves, J. S. J., Hutchings, G. J., Joyner, R. W., and Kiely, C. J., *Catal. Today* **13**, 401 (1992).
13. Schluger, A. L., Gale, J. D., and Catlow, C. R. A., *J. Phys. Chem*. **96**, 1089 (1992).
14. Lunsford, J. H., Cisneros, M. D., Hinson, P. G., Tong, Y., and Zhang, H., *Faraday. Discuss. Chem. Soc.* **87**, 13 (1989).
15. Otsuka, K., Jinno, K., and Morikawa, A., *Chem. Lett.* 499 (1985).
16. Sinev, M. Y., Tyulenin, Y. P., and Rozentuller, B. V., *Kinet. Catal.* **32**, 807 (1991).
17. Burrows, A., Blick, K. H., Devenish, R. W., Hutchings, G. J., Joyner, R. W., Kiely, C. J., and Sinev, M. Y., *Stud. Surf. Sci. Catal.* **81**, 223 (1994).
18. Wyckoff, R. W. G., "Crystal Structures," Vol. 2. Wiley (1986).
19. Scofield, J. H., *J. Electron Spectroscopy Relat. Phenom*. **8**, 129 (1976).
20. Burrows, A., Ph.D. thesis, University of Liverpool, 1995.
21. Kingery, W. D., Bowen, H. K., and Uhlmann, D. R., "Introduction to Ceramics," Wiley, New York, 1976.
22. Burrows, A., Kiely, C. J., Devenish, R. W., Hargreaves, J. S. J., Hutchings, G. J., Joyner, R. W., and Sinev, M. Y., *Mat. Res. Soc. Symp.* **344**, 39 (1994).
23. Burrows, A., Kiely, C. J., Hargreaves, J. S. J., Joyner, R. W., Hutchings, G. J., and Sinev, M. Y., *J. Catal.*